

# Analysis of spatial spectral features of dynamic contrast-enhanced brain magnetic resonance images for studying small vessel disease



# Analysis of spatial spectral features of dynamic contrast-enhanced brain magnetic resonance images for studying small vessel disease

Jose Bernal[1 [0000−0003−3167−5134]], Maria del C. Valdés-Hernández[1 [0000−0003−2771−6546]], Javier Escudero[2 [0000−0002−2105−8725]], Paul A. Armitage[3 [0000−0001−5710−567X]], Stephen Makin[4 [0000−0001−8701−9043]], Rhian M. Touyz[4 [0000−0003−0670−0887]], and Joanna M. Wardlaw[1 [0000−0002−9812−6642]]

[1] Centre for Clinical Brain Sciences, University of Edinburgh, Edinburgh, UK
{jose.bernal, m.valdes-hernan}@ed.ac.uk
[2] School of Engineering, Institute for Digital Communications, University of Edinburgh, Edinburgh, UK
[3] Academic Unit of Radiology, University of Sheffield, Sheffield, UK
[4] Institute of Cardiovascular and Medical Sciences, University of Glasgow, Glasgow, UK

**Abstract.** Cerebral small vessel disease (SVD) comprises all the pathological processes affecting small brain vessels and, consequently, damaging white and grey matter. Although the cause of SVD is unknown, there seems to be a dysfunction of the small vessels. In this paper, we propose a framework comprising tissue segmentation, spatial spectral feature extraction, and statistical analysis to study intravenous contrast agent distribution over time in cerebrospinal fluid, normal-appearing and abnormal brain regions in patients with recent mild stroke and SVD features. Our results show the potential of the power spectrum for the analysis of dynamic contrast-enhanced brain MRI acquisitions in SVD since significant variation in the data was related to vascular risk factors and visual clinical variables that characterise the burden of SVD features. Thus, our proposal may increase sensitivity to detect subtle features of small vessel dysfunction. A public version of our framework can be found at `https://github.com/joseabernal/DynamicBrainMRIAnalysis.git`.

**Keywords:** Spatial spectral analysis · Functional principal component analysis · Dynamic brain magnetic resonance image · Cerebral small vessel disease

## 1 Introduction

Small vessel disease of the brain (SVD) comprises multiple pathological processes affecting small cerebral arteries leading to damage of white and grey matter (WM and GM, respectively) [17]. SVD is a serious problem that has been associated with cognitive decline, physical fragility, depression, dementia, and stroke [17].

Although the cause(s) of SVD remain unclear, there seems to be dysfunction of the small vessels. This issue may be studied using dynamic contrast-enhanced MRI (DCE-MRI). However, factors such as scanner signal drift, tissue variations, and imaging artefacts introduce systematic errors hampering assessing small vessel dysfunction accurately.

Dynamic brain MRI acquisitions are commonly temporally sparse and spatially dense. Thus, proposals usually find alternative data representations to reduce the dimensionality of the data while retaining critical information [7, 8]. The power spectrum [1] is a common approach in digital signal processing to describe the strength of frequency components into the overall signal. It has been successfully applied in dynamic susceptibility contrast brain MRI to characterise neurophysiological and hemodynamic patterns of Alzheimer's disease [8]. We hypothesise that spatial spectral feature analysis of dynamic post-contrast signal changes can identify tissue differences in tissues that relate to the burden of SVD features and clinical factors.

In this paper, we propose a framework to study contrast signal-time trajectory in healthy and pathological brain regions in dynamic contrast-enhanced (DCE) brain MRI acquisitions. The framework comprises segmentation, spatial spectral and functional data analyses, and statistical group comparison. The contributions of this work are: (i) we showcase a fully functional framework to analyse DCE-MRI acquisitions using spatial spectral and functional data analyses jointly, and (ii) we describe an application of our framework to the study of DCE-MRI signals of a relatively large cohort ($n = 201$) with various extents of SVD features.

## 2 Methods

### 2.1 Analysis framework

The processing pipeline consists of three steps. First, all regions of interest are segmented for each patient in the cohort. Second, signals measured in each brain region are described using the power spectrum. Third, spectral features are examined using statistical tests to establish whether they vary with any of the clinical variables. A scheme of the pipeline applied per patient is displayed in Fig. 1. Further details of each step are provided in the following sections.

### 2.2 Subjects and clinical scores

We used data from a prospective study of patients with recent mild stroke and SVD features ($n = 201$ subjects, 79 women). The sample clinical characteristics have been published previously [13, 15]; those relevant to this study are summarised in Table 1. The DCE-MRI acquisition parameters have been detailed in [6]. Patients were scanned at approximately one month after the first stroke presentation. Following a pre-contrast acquisition, an intravenous bolus injection of gadolinium was administered with the start of 20 further acquisitions

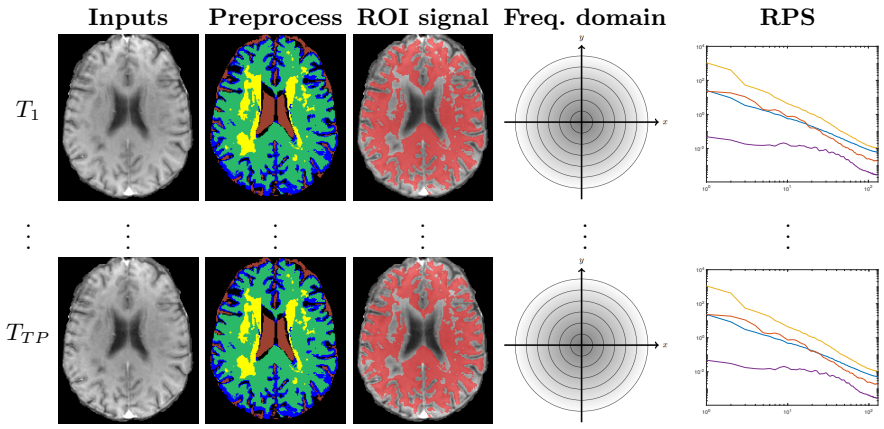


Fig. 1: High level schematic of our processing pipeline per patient. RPS refers to the radial power spectrum. On the left, $T_1$, $T_2$, ..., $T_{TP}$ refer to each one of the time points. The inputs are the post intravenous gadolinium contrast brain MRI sequences, T1-w, T2-w, FLAIR and the susceptibility-weighted images. Initially, we segment the regions of interest using the different imaging sequences. Then, we study the dynamic signals per region of interest using the obtained segmentation masks. Next, we convert the signals to the spatial frequency domain using the Fourier transform. Finally, we average power values over all frequencies in concentric rings of a specific width. In the RPS column, the lines represent the RPS compute for cerebrospinal fluid (blue), deep grey matter (orange), normal-appearing white matter (yellow), and white matter hyperintensities (purple).

with a temporal resolution of 73s, leading to a DCE-MRI duration of about 24 minutes ($\approx$ 21 time points). We considered only those after the $4^{th}$ time point to minimise initial perfusion effects that occur before the contrast agent is well mixed within the blood/intravascular compartment.

The following baseline clinical and demographic variables were obtained from the study database: biological sex (m/f), smoker (y/n), diabetes (y/n), hyperlipidemia (y/n) defined as a previous diagnosis, or diagnoses at time of stroke of a total cholesterol over 5mmol/L, hypertension (y/n) defined as a previous history of hypertension, or hypertension diagnosed at presented of stroke. Additionally, we considered visual clinical ratings recorded at inclusion. In particular, we utilised Fazekas [2], basal ganglia perivascular spaces (BGPVS) [10], and total SVD [12] scores to account for the location, presence and size of WMH, the existence of enlarged PVS on the basal ganglia, and the burden of four MRI features of the SVD (lacunes, microbleeds, PVS, and WMH). We summed up periventricular and deep WM scores to obtain a total Fazekas score that ranged from zero to six [4, 14]. A senior and experienced neuroradiologist generated all visual scores.

Table 1: Clinical variables from the sample relevant for this study. The first column lists the variables of interest, the second one shows the frequency and approximated relative frequency of that variable.

| **Clinical variable** | **No. of patients (% of the total)** |
|---|---|
| Hypertension | 150 (74.6%) |
| Diabetes | 25 (12.4%) |
| Hyperlipidemia | 120 (59.7%) |
| Smoker | 130 (64.7%) |
| Fazekas score | |
| 0 | 6 (3.0%) |
| 1 | 16 (8.0%) |
| 2 | 74 (36.8%) |
| 3 | 23 (11.4%) |
| 4 | 32 (14.9%) |
| 5 | 20 (10.0%) |
| 6 | 32 (15.9%) |
| BGPVS score | |
| 0 | 3 (1.5%) |
| 1 | 102 (50.7%) |
| 2 | 54 (26.9%) |
| 3 | 26 (12.9%) |
| 4 | 16 (8.0%) |
| Total SVD score | |
| 0 | 67 (33.3%) |
| 1 | 48 (23.9%) |
| 2 | 46 (22.9%) |
| 3 | 27 (13.4%) |
| 4 | 13 (6.5%) |

### 2.3 Segmentation of regions of interest

We examined four regions of interest comprising both normal-appearing and abnormal brain regions: cerebrospinal fluid (CSF), deep GM (DGM), normal-appearing WM (NAWM), and WMH. Each segmentation was performed following the protocol described in [13]. Trained analysts double-checked and manually edited all segmentation masks under the supervision of an experienced neuroradiologist. To avoid partial volume effects, we eroded the resulting binary masks. The segmentation methods were evaluated previously against manually obtained reference segmentations, in images acquired with similar scanning parameters and on the same scanner like the ones this study uses [13]. On 150 individuals, the mean difference for ICV segmentations was 2.7% (95% CI $\pm$7%). On 20 individuals, the Jaccard Index was 0.98 (95% CI = $\pm$0.03) for WM, 0.46 (95% CI = $\pm$0.12) for CSF, and 0.61 (95% CI = $\pm$0.37) for WMH. In a test-retest analysis on 14 cases comprising volunteers and patients with mild non-disabling stroke, the coefficient of variation for repeated measurements of the segmentation tech-

nique was 0.21 [5]. Further information concerning inter-analyst agreements can be found in [13].

### 2.4 Power spectral features of the regions of interest

We characterised the signals gauged within normal-appearing and abnormal tissues in dynamic brain MRI acquisitions using the radial power spectrum (RPS) [1]. The steps to compute it for each time point and each region of interest are three-fold. First, we selected the signal in the region of interest using the segmentation masks. Second, we used the 2D discrete Fourier transform to obtain a representation of each axial slice forming the region of interest in the frequency domain. Let $I \in \mathbb{R}^{N \times N \times K}$ be a brain MR volume with $K$ axial slices and $f_k(x, y)$ be its $k$-th axial slice, the corresponding discrete Fourier transform for each slice, $F_k(u, v)$, is expressed as follows

$$F_k(u,v) = \sum_{i=0}^{N-1} \sum_{j=0}^{N-1} f_k(i,j) \exp\left(-2\iota\pi\left(\frac{ui}{N} + \frac{vj}{N}\right)\right). \tag{1}$$

Third, we computed the magnitude spectra and averaged all the frequencies over concentric rings of width 1 using the following formula

$$R^{(s)} = \frac{1}{K} \sum_{k=1}^{K} \frac{1}{2\pi} \int_0^{2\pi} |F_k(s\,\cos(\theta), s\,\sin(\theta))|\, d\theta, \tag{2}$$

where $s = \sqrt{u^2 + v^2}$ and $\theta = \tan^{-1}\left(\frac{v}{u}\right)$ are polar coordinates. For each time point and each region of interest, the signal was described using 129 frequencies.

### 2.5 Functional data analysis

Each one of the elements of the RPS can be seen as a function in time. In such a way, we could find the eigenvalues and eigenfunctions that better describe the different observations. We followed the method proposed by Happ & Greven [3]. Let $D = 129$ be the number of elements under study at each time point, $P = 201$ the number of patients, and $R = \{R^{(1)}, ..., R^{(D)}\}$ the set of elements, each of them described by the corresponding measurements, $r_1^{(j)}$, $r_2^{(j)}$, ..., $r_P^{(j)}$, the overall process is four-fold. First, each variable was centred by subtracting its mean value. Second, eigenfunctions and scores were calculated for each variable using the functional PCA. The principal component functions were obtained constructively by finding orthogonal functions $\Phi_k^{(j)}$, $k = 1, ..., M^{(j)}$, for which principal component scores $\xi_{ik}^{(j)}$, $i = 1, ..., P$, mathematically expressed as

$$\xi_{ik}^{(j)}(t) = \int \Phi_k^{(j)}(t)\, r_i^{(j)}(t) dt, \tag{3}$$

maximised $\sum_i {\xi_{ik}^{(j)}}^2$, subject to $||\Phi_k^{(j)}||^2 = 1$, were $t \in [4, 5, 6, ..., 21]$ represents each time point. We set $M^{(j)}$ to five as resulting eigenvectors accounting for

the 99% of the univariate variation. Third, all of these scores $\xi_{ik}^{(j)}$ were arranged in a matrix form, $\Xi \in \mathbb{R}^{P \times \sum M^{(j)}}$, such that the $i^{th}$ row contained $(\xi_{i1}^{(1)}, ..., \xi_{iM^{(1)}}^{(1)}, ..., \xi_{i1}^{(p)}, ..., \xi_{iM^{(p)}}^{(p)})$. Fourth, scores were calculated using eigenanalysis on the covariance matrix of $\Xi$. We resorted to using the first three modes of variation which explained around the 99% of the data variation. The output at this stage was a score for per mode of variation for each subject.

### 2.6 Validation against clinical parameters

We used the Kruskal-Wallis test to determine whether the features vary with any of the clinical parameters. We verified that the analysed variables were not normally distributed using the Shapiro-Wilk test. The null hypothesis was that subjects with different clinical scores exhibit similar feature values. We computed the test in R version 3.5.1 and corrected the $p$-values for multiple comparisons using the Benjamini-Hochberg false discovery rate control method.

## 3 Experiments and results

The application of our framework to the case study was performed as follows. We segmented each of the 201 DCE-MRI scans, measured the signal gauged in each region of interest using the resulting tissue masks, calculated the RPS of each time point and each region of interest, and extracted spectral measurements. Once we obtained the spectral features for each patient, we compared them using statistical analysis to explore whether they vary with clinical variables. An example of the radial power spectra calculated from signals gauged in the WM hyperintense (WMH) regions with the lowest and highest WMH burden is shown in Fig. 2. As it can be observed, the two groups of patients exhibit different spectra.

We compared two functional data analysis approaches: a time-averaged and a dynamic RPS, the latter taking signal over time into account. The corresponding significance values obtained from the Kruskal-Wallis test are presented in Table 2 and Table 3, respectively. Apart from considering the RPS of each region of interest independently, we analysed them jointly as well. The corresponding results are displayed in the column "All" of both tables. In most of the cases, both approaches coincided. However, there were slight differences. The spectral features computed in the CSF region varied with Fazekas scores, but the method considering the temporal dimension exhibited stronger evidence ($p$-value $< 0.0001$) than the time-averaged scheme ($p$-value $< 0.001$). Similarly, the scores yielded by the dynamic RPS showed more evidence of variation with the burden of SVD features in the DGM region ($p$-value $< 0.05$) compared to the time-averaged RPS ($p$-value $> 0.05$). These outcomes suggest that the temporal component is of relevance, consistent with our hypothesis [16].

The power spectrum (expressed through PC1, PC2, and PC3) varied ($p$-value $< 0.05$) when grouped by visual clinical ratings regardless of the region of interest, indicating that burden of SVD influenced the spectral findings. The

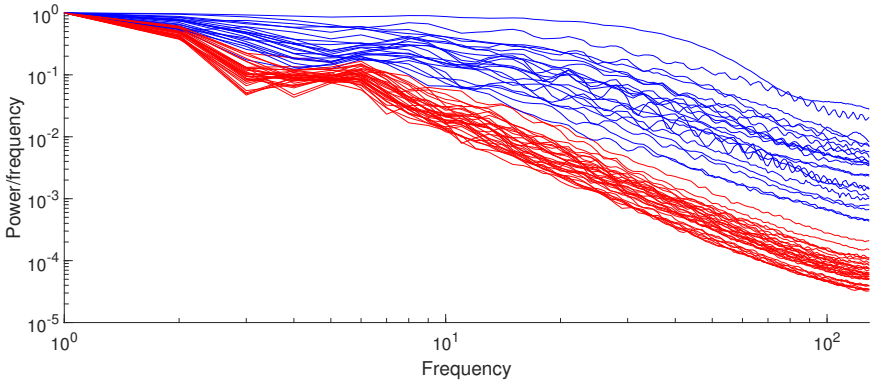


Fig. 2: Radial power spectra calculated from real signals in the white matter hyperintense regions for patients with Fazekas score 6 (red) and Fazekas score 0 and 1 (blue). Each line corresponds to the spectrum of a patient in the time point 4. The values were normalised by the DC value for visualisation purposes.

measurements gathered from all the regions of interest varied significantly with biological sex ($p$-value $< 0.05$), overall WMH burden ($p$-value $< 0.001$), BGPVS scores ($p$-value $< 0.05$), and total SVD ($p$-value $< 0.001$). An example of the distribution of principal component scores in CSF, DGM, and NAWM, according to deep and periventricular Fazekas scores, is shown in Fig. 3. The tendency overall was that scores decreased significantly ($p$-value $< 0.05$) with increased WMH burden.

The power spectrum appeared to change concerning covariates such as diabetes, hypertension, and hyperlipidemia ($p$-value $< 0.05$), but the variations were observed in specific regions: hypertension in NAWM, WMH and All, diabetes in WMH and All, and hyperlipidemia in DGM. When stratified by smoker vs non-smoker, the signals did not differ ($p$-value $> 0.05$). In general, the power spectrum calculated from normal-appearing and abnormal regions of interest varied significantly mostly with clinical SVD ratings.

In terms of computational time, the manual rectification of the segmentation boundaries consumed most of the time, being it reported to take between 20 and 60 minutes per patient for WM and WMH depending on the expertise of the analyst. [13]. The calculation of the RPS per patient can take up to one minute, and the computation of the PCA scores for a region of interest for all 201 patients takes approximately two minutes on a Microsoft Windows 10 machine with 8GB RAM (i5-4590 CPU Intel(R) processor @ 3.30 GHz).

## 4 Discussion

In this paper, we propose, for the first time, a framework incorporating power spectrum analysis to study dynamic brain MRI signals of brain-related pathological processes. Our team implemented the segmentation protocols and methods,

Table 2: Kruskal-Wallis test results obtained when comparing the functional principal component (PC) scores extracted from the time-averaged RPS of subjects grouped by clinical variables. The percentages under each one of the PC correspond to the portion of data variability each of them describe. The column "All" refers to the result obtained when analysing principal components of all regions of interest jointly. Significant values are shown in bold. For each univariate test, the number of samples was 201.

| **Clinical variable** | **CSF** | | | **DGM** | | | **NAWM** | | | **WMH** | | | **All** | | |
|---|---|---|---|---|---|---|---|---|---|---|---|---|---|---|---|
| | PC1 | PC2 | PC3 | PC1 | PC2 | PC3 | PC1 | PC2 | PC3 | PC1 | PC2 | PC3 | PC1 | PC2 | PC3 |
| | 98% | 1% | 1% | 98% | 1% | 1% | 98% | 1% | 1% | 99% | 1% | 1% | 84% | 15% | 1% |
| Biological sex | **0.003** | **0.001** | **0.001** | **0.002** | **0.031** | **0.008** | **0.021** | **0.032** | **0.018** | 0.562 | 0.379 | 0.297 | **0.009** | 0.137 | **0.001** |
| Smoker | 0.386 | 0.949 | 0.184 | 0.055 | 0.238 | 0.063 | 0.281 | 0.310 | 0.330 | 0.274 | 0.392 | 0.297 | 0.195 | 0.211 | 0.733 |
| Diabetes | 0.060 | 0.697 | **0.042** | 0.825 | 0.874 | 0.892 | 0.281 | 0.168 | 0.287 | **0.032** | 0.392 | 0.596 | 0.259 | 0.938 | **0.004** |
| Hyperlipidemia | 0.785 | 0.921 | 0.618 | **0.035** | 0.460 | 0.136 | 0.374 | 0.495 | 0.414 | 0.508 | 0.392 | 0.297 | 0.259 | 0.124 | 0.503 |
| Hypertension | 0.060 | 0.380 | **0.047** | 0.471 | 0.874 | 0.752 | **0.021** | **0.012** | **0.022** | **0.021** | 0.379 | 0.297 | **0.019** | 0.938 | 0.091 |
| Fazekas | 0.060 | 0.921 | **0.002** | **0.007** | 0.238 | 0.091 | **0.001** | **0.001** | **0.001** | **0.001** | **0.001** | **0.001** | **0.001** | 0.137 | **0.001** |
| BGPVS | 0.060 | 0.697 | **0.002** | 0.106 | 0.419 | 0.313 | **0.021** | **0.012** | **0.034** | **0.001** | **0.013** | **0.001** | **0.006** | 0.162 | **0.001** |
| Total SVD | 0.090 | 0.921 | **0.002** | 0.054 | 0.669 | 0.313 | **0.001** | **0.001** | **0.001** | **0.001** | **0.001** | **0.001** | **0.001** | 0.137 | **0.001** |

the computation of the power spectrum features, and the integration of each processing module into the proposed framework. In particular, we applied our processing pipeline to the study of SVD tissue changes using DCE-MRI acquisitions. The power spectrum gauged from normal-appearing and abnormal brain regions of a population with features of SVD of differing extents was analysed to explore whether patients with biological sex, hypertension and visual ratings (namely Fazekas, BGPVS, total SVD scores) exhibited distinctive spectra. To the best of our knowledge, this is the first time that the power spectrum has been examined for this purpose in a relatively large cohort ($n = 201$) with a wide range of SVD features. Of note, we applied our framework to the study of DCE-MRI signals. Nonetheless, this does not prevent it from being used for analysing other dynamic and non-dynamic brain MR acquisitions.

Due to the relative temporal sparsity and spatial density of the dynamic brain MRI acquisitions, the number of techniques that can be used to process them is reduced. Thus, finding adequate alternative representations is crucial. In this paper, we explored the spectral density for studying dynamic brain MRI signals in SVD. According to our evaluation results, we found that spectral features of the DCE-MRI acquisitions vary significantly with biological sex, hypertension, and clinical visual ratings (namely, Fazekas, BGPVS, and total SVD scores). This outcome suggests that the use of the power spectrum is suitable for examining these types of acquisitions.

We evaluated two approaches for extracting features out of the RPS. The first one contemplated computing the mean RPS over time and studying it through univariate functional PCA. The second one consisted of describing each element of the dynamic RPS through multivariate functional PCA. In both cases, we retrieved the scores resulting in the direction of the first three modes of variation. We observed that the two approaches coincide most of the time. However, as the former method summarises the temporal changes in the data, the latter should

Table 3: Kruskal-Wallis test results obtained when comparing the functional principal component (PC) scores extracted from the RPS of subjects grouped by clinical variables. The percentages under each one of the PC correspond to the portion of data variability each of them describe. The column "All" refers to the result obtained when analysing principal components of all regions of interest jointly. Significant values are shown in bold. For each univariate test, the number of samples was 201.

| **Clinical variable** | **CSF** | | | **DGM** | | | **NAWM** | | | **WMH** | | | **All** | | |
|---|---|---|---|---|---|---|---|---|---|---|---|---|---|---|---|
| | PC1 | PC2 | PC3 | PC1 | PC2 | PC3 | PC1 | PC2 | PC3 | PC1 | PC2 | PC3 | PC1 | PC2 | PC3 |
| | 96% | 3% | 1% | 90% | 8% | 2% | 94% | 5% | 1% | 93% | 5% | 1% | 84% | 15% | 1% |
| Biological sex | **0.001** | **0.001** | 0.563 | **0.001** | **0.001** | 0.849 | **0.019** | **0.001** | 0.573 | 0.554 | 0.273 | 0.102 | 0.060 | 0.121 | **0.001** |
| Smoker | 0.313 | 0.209 | 0.939 | 0.066 | 0.110 | 0.769 | 0.292 | 0.346 | 0.263 | 0.257 | 0.985 | 0.740 | 0.216 | 0.239 | 0.456 |
| Diabetes | 0.051 | 0.991 | 0.376 | 0.828 | 0.317 | 0.607 | 0.292 | 0.319 | 0.941 | **0.035** | 0.985 | 0.979 | 0.251 | 0.994 | **0.048** |
| Hyperlipidemia | 0.784 | 0.209 | 0.563 | **0.044** | 0.980 | 0.607 | 0.403 | 0.425 | 0.573 | 0.481 | 0.985 | 0.583 | 0.251 | 0.098 | 0.862 |
| Hypertension | 0.051 | 0.991 | 0.563 | 0.486 | 0.801 | 0.849 | **0.023** | 0.708 | 0.538 | **0.019** | 0.261 | 0.372 | **0.017** | 0.994 | 0.686 |
| Fazekas | **0.041** | 0.257 | **0.001** | **0.009** | **0.026** | 0.941 | **0.001** | **0.001** | 0.573 | **0.001** | **0.001** | **0.001** | **0.001** | 0.098 | **0.001** |
| BGPVS | **0.041** | 0.828 | **0.001** | 0.124 | **0.026** | 0.159 | **0.023** | **0.001** | 0.751 | **0.001** | **0.001** | 0.102 | 0.066 | 0.142 | **0.001** |
| Total SVD | 0.051 | 0.164 | **0.001** | 0.067 | **0.013** | 0.496 | **0.001** | **0.001** | 0.836 | **0.001** | **0.001** | **0.001** | **0.001** | 0.121 | **0.001** |

be preferred. Our experimental results support this claim and are consistent with our hypothesis.

The spatial spectral features extracted from the signal in the NAWM region differed significantly with SVD features and their extents. This observation agrees with previous finding in which the differentiation between "normal" and "abnormal" tissues becomes less evident with increased age and SVD feature severity [14]. Interestingly, a small percentage of the variations of the spectral features in the CSF region differed significantly with SVD features and their extents. This situation might be related to leakage of gadolinium in CSF with increased SVD burden [14]. The Fazekas score has been found to be associated with increasing BBB leakage [9, 16] and as the spectral features of patients grouped by this visual rating were statistically different, this outcome suggests that our framework can be used in the study of small vessel dysfunction.

Differences regarding biological sex (and presumably brain size as well) are expected as a direct consequence of the scaling theorem of the Fourier transform in which the size of the region of interest is linked to its Fourier representation [11]. Thus, the size of brain structures within a region of interest is expected to be, in principle, encoded in the spectral features used. This problem may be alleviated by processing the regions of interest in a short-time Fourier transform or sliding-window processing fashion or by manually selecting matching and relevant regions of interest with exactly the same area/volume on all scans. In the future, we plan to explore alternatives in these regards.

In the present work, we showed that a strategy based on the study of the power spectrum could be used to investigate dynamic post-contrast signal changes in tissues that relate to the extents of SVD features, vascular risk factors and clinical visual ratings. The outcomes of our experiments add confidence to previous findings in which DCE-MRI signals from patients with different age, health status, and premorbid brain condition exhibited different tendencies [16]. For

instance, a pre- and post-contrast texture analysis concluded that local signal variations, measured in terms of homogeneity and contrast, differed significantly depending on the extents of SVD features [14]. Future work should consider understanding what physiopathological processes cause these power spectrum variations and which aspects of the spectrum are different among patient groups.

## Acknowledgements

JB holds an MRC Precision Medicine Doctoral Training Programme studentship from the University of Edinburgh. This work was supported by the Row Fogo Charitable Trust (MVH) grant no. BRO-D.FID3668413, Wellcome Trust (patient recruitment, scanning, primary study Ref No. WT088134/Z/09/A), Fondation Leducq (Perivascular Spaces Transatlantic Network of Excellence), and EU Horizon 2020 (SVDs@Target) and the MRC UK Dementia Research Institute (Wardlaw programme). The authors thank participants in the study, the radiographers and staff at the Edinburgh Imaging Facilities (`www.ed.ac.uk/clinical-sciences/edinburgh-imaging/research/facilities-and-equipment/edinburgh-imaging-facilities`), the UK Dementia Research Institute at the University of Edinburgh, and the Row Fogo Centre for Ageing and the Brain.

## References

1. Chapter 3 power spectrum and its applications. In: Naidu, P.S., Mathew, M. (eds.) Analysis of Geophysical Potential Fields, Advances in Exploration Geophysics, vol. 5, pp. 75 – 143. Elsevier (1998)
2. Fazekas, F., Niederkorn, K., Schmidt, R., Offenbacher, H., Horner, S., Bertha, G., Lechner, H.: White matter signal abnormalities in normal individuals: correlation with carotid ultrasonography, cerebral blood flow measurements, and cerebrovascular risk factors. Stroke **19**(10), 1285–1288 (1988)
3. Happ, C., Greven, S.: Multivariate functional principal component analysis for data observed on different (dimensional) domains. Journal of the American Statistical Association pp. 1–11 (2018)
4. Hernández, M.D.C.V., Chappell, F.M., Maniega, S.M., Dickie, D.A., Royle, N.A., Morris, Z., Anblagan, D., Sakka, E., Armitage, P.A., Bastin, M.E., et al.: Metric to quantify white matter damage on brain magnetic resonance images. Neuroradiology **59**(10), 951–962 (2017)
5. Hernández, M.d.C.V., Ferguson, K.J., Chappell, F.M., Wardlaw, J.M.: New multispectral MRI data fusion technique for white matter lesion segmentation: method and comparison with thresholding in FLAIR images. European radiology **20**(7), 1684–1691 (2010)
6. Heye, A.K., Thrippleton, M.J., Armitage, P.A., Hernández, M.d.C.V., Makin, S.D., Glatz, A., Sakka, E., Wardlaw, J.M.: Tracer kinetic modelling for DCE-MRI quantification of subtle blood–brain barrier permeability. Neuroimage **125**, 446–455 (2016)
7. Khalifa, F., Soliman, A., El-Baz, A., Abou El-Ghar, M., El-Diasty, T., Gimel'farb, G., Ouseph, R., Dwyer, A.C.: Models and methods for analyzing DCE-MRI: A review. Medical physics **41**(12) (2014)

8. Mattia, D., Babiloni, F., Romigi, A., Cincotti, F., Bianchi, L., Sperli, F., Placidi, F., Bozzao, A., Giacomini, P., Floris, R., et al.: Quantitative EEG and dynamic susceptibility contrast MRI in Alzheimer's disease: a correlative study. Clinical neurophysiology **114**(7), 1210–1216 (2003)
9. Muñoz Maniega, S., Chappell, F.M., Valdés Hernández, M.C., Armitage, P.A., Makin, S.D., Heye, A.K., Thrippleton, M.J., Sakka, E., Shuler, K., Dennis, M.S., et al.: Integrity of normal-appearing white matter: influence of age, visible lesion burden and hypertension in patients with small-vessel disease. Journal of Cerebral Blood Flow & Metabolism **37**(2), 644–656 (2017)
10. Potter, G., Doubal, F., Jackson, C., Sudlow, C., Dennis, M., Wardlaw, J.: Associations of clinical stroke misclassification (clinical-imaging dissociation) in acute ischemic stroke. Cerebrovascular Diseases **29**(4), 395–402 (2010)
11. Smith, J.O.: Mathematics of the Discrete Fourier Transform (DFT). W3K Publishing (2007)
12. Staals, J., Makin, S.D., Doubal, F.N., Dennis, M.S., Wardlaw, J.M.: Stroke subtype, vascular risk factors, and total MRI brain small-vessel disease burden. Neurology **83**(14), 1228–1234 (2014)
13. Valdés Hernández, M.d.C., Armitage, P.A., Thrippleton, M.J., Chappell, F., Sandeman, E., Muñoz Maniega, S., Shuler, K., Wardlaw, J.M.: Rationale, design and methodology of the image analysis protocol for studies of patients with cerebral small vessel disease and mild stroke. Brain and behavior **5**(12), e00415 (2015)
14. Valdés Hernández, M.d.C., González-Castro, V., Chappell, F.M., Sakka, E., Makin, S., Armitage, P.A., Nailon, W.H., Wardlaw, J.M.: Application of texture analysis to study small vessel disease and blood–brain barrier integrity. Frontiers in neurology **8**, 327 (2017)
15. Wardlaw, J.M., Chappell, F.M., Hernández, M.d.C.V., Makin, S.D., Staals, J., Shuler, K., Thrippleton, M.J., Armitage, P.A., Muñoz-Maniega, S., Heye, A.K., et al.: White matter hyperintensity reduction and outcomes after minor stroke. Neurology **89**(10), 1003–1010 (2017)
16. Wardlaw, J.M., Makin, S.J., Hernández, M.C.V., Armitage, P.A., Heye, A.K., Chappell, F.M., Munoz-Maniega, S., Sakka, E., Shuler, K., Dennis, M.S., et al.: Blood-brain barrier failure as a core mechanism in cerebral small vessel disease and dementia: evidence from a cohort study. Alzheimer's & Dementia **13**(6), 634–643 (2017)
17. Wardlaw, J.M., Smith, C., Dichgans, M.: Mechanisms of sporadic cerebral small vessel disease: insights from neuroimaging. The Lancet Neurology **12**(5), 483–497 (2013)

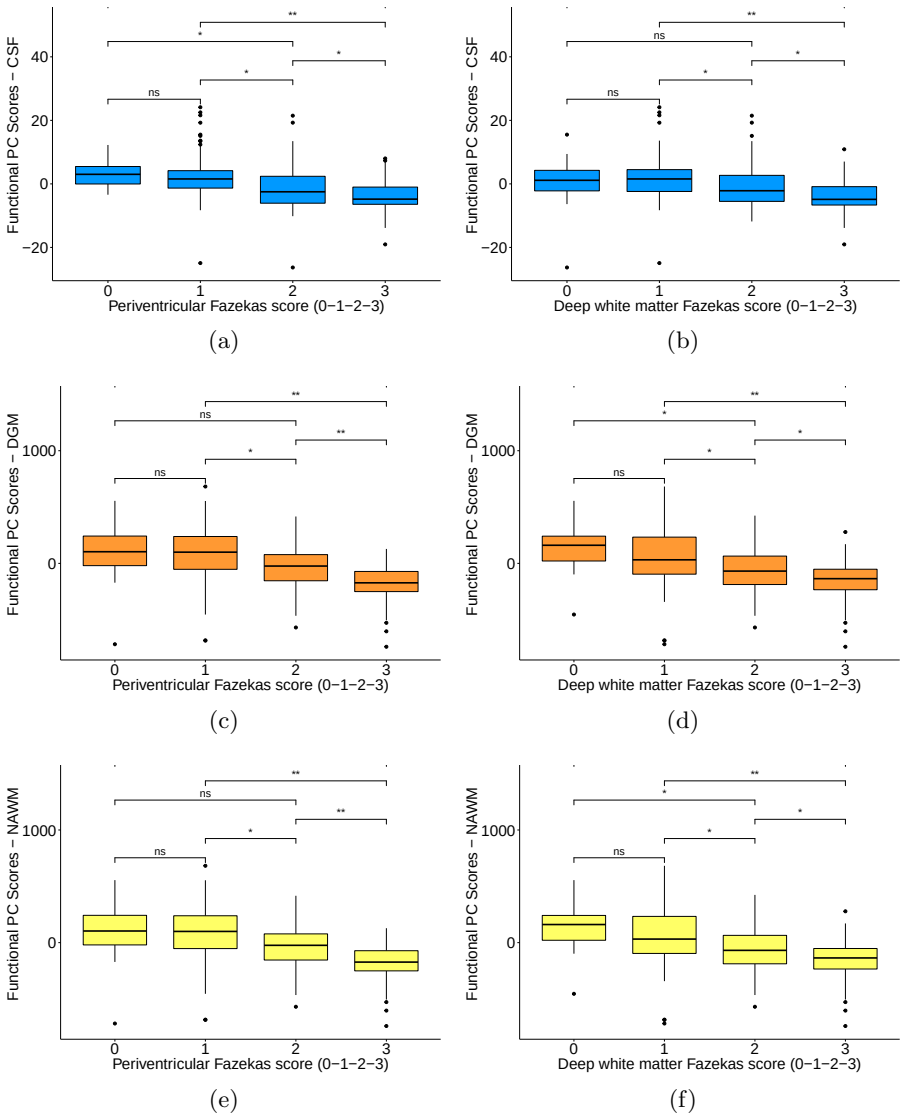


Fig. 3: Distribution of PCA scores obtained for the CSF (blue), DGM (orange), and NAWM (yellow) regions grouped by the Fazekas periventricular WM (left) and deep WM (right) scores of the patients. The scores correspond to PC3 for CSF, PC2 for DGM, and PC2 for NAWM. Significant differences between pairs of groups have been highlighted with $^{*}p < 0.05$ $^{**}p < 0.001$.